Molecular dynamics simulations of the structural and dynamic properties of graphite-supported bimetallic transition metal clusters

Subramanian K. R. S. Sankaranarayanan, Venkat R. Bhethanabotla,* and Babu Joseph
Sensors Research Laboratory, Chemical Engineering Department, University of South Florida, Tampa, Florida 33620-5350, USA
(Received 10 May 2005; revised manuscript received 14 September 2005; published 4 November 2005)

Molecular dynamics simulations were carried out for Pd-Pt, Pd-Rh, and Pd-Cu nanoclusters supported on a static graphite substrate using the quantum Sutton-Chen potential for the metal-metal interactions. The graphite substrate was represented as layers of fixed carbons sites and modeled with the Lennard-Jones potential model. Metal-graphite interaction potentials obtained by fitting experimental cohesive energies were utilized. Monte Carlo simulations employing the bond order simulation model were used to generate initial configurations. The melting temperatures for bimetallic nanoclusters of varying composition were estimated based on variations in thermodynamic properties such as potential energy and heat capacity. Melting transition temperatures were found to decrease with increasing Cu (for Pd-Cu) and Pd (for Pd-Pt and Pd-Rh) concentrations and are at least 100 to 200 K higher than those of the same-sized free clusters. Density distributions perpendicular to the surface and components of the velocity autocorrelation functions in the plane of the surface indicate that one of the metals in the bimetallic nanoclusters wets the graphite surface more, and that this weak graphite substrate is able to structure the melted fluid in the first few monolayers. The wetting characteristics are dictated by the delicate balance between metal-metal and metal-graphite interactions. Components of velocity-autocorrelation functions characterizing diffusion of constituent atoms in these bimetallics suggest greater out-of-plane movement, which increases with Cu (for Pd-Cu) and Pd (for Pd-Rh and Pd-Pt) concentrations. Deformation parameters showed that the core (Pd in Pd-Cu, Rh in Pd-Rh and Pt in Pd-Pt) atoms diffuse out and the surface-segregated (Cu in Pd-Cu, Pd in Pd-Rh and Pd-Pt) atoms diffuse into the nanoclusters upon melting. Near linear dependence of melting temperature on composition was found for unsupported clusters in our recent work, which results from the balance between the extent of surface melting and the radius of remaining solid core. Nonlinear dependence was found in these supported clusters, as a result of reduced surface melting at higher Pd concentrations, due to the substrate effect. Shell-based diffusion coefficients for layers perpendicular to the graphite substrate suggest surface melting to start from the cluster surface experiencing least influence of the graphite field. Surface melting was seen in all three nanoclusters, with calculated bond orientational order parameters revealing the order of Pd-Cu > Pd-Pt > Pd-Rh, for onset of melting. Cluster snapshots on the graphite substrate and calculated cluster diffusion coefficients indicate these nanoclusters to diffuse as single entities with very high diffusivities, consistent with experimental observations.

DOI: 10.1103/PhysRevB.72.195405 PACS number(s): 36.40.Ei, 65.80.+n, 64.70.Dv

I. INTRODUCTION

Metal nanoparticles exhibit physical, chemical, and electrical properties that are different from those of bulk materials or single molecules.[1] The unique properties imparted to nanoparticles by the large fraction of surface atoms help them find applications in areas such as heterogeneous catalysis, sensors, and microelectronics. The size, shape, and composition of these nanoparticles are known to affect their physical and chemical properties. In sensing applications, for instance, the increased surface area leads to improved sensitivity, selectivity, and speed of response. As an example, Pd and its alloy nanoparticles have found use in hydrogen sensing.[2,3] Literature suggests that bimetallics exhibit superior properties in comparison to their single-metal counterparts.[4] In catalysis and sensing applications, bimetallic nanoparticles supported on substrates such as alumina, ceria, carbon, quartz, or lithium niobate are commonly used. The behavior of nanoclusters under the influence of a substrate is different from that of isolated nanoclusters.[5–8] The properties in these cases are dependent not only on the particle size and surface composition, but also on the surface morphology and nature of metal-substrate interaction. The key to all potential applications lies in a thorough understanding of thermal, structural, and dynamic properties of these nanoparticles, especially under the influence of a substrate. Recent advances in experimental techniques[9,10] as well as the insights gained by using first-principles calculations such as density functional theory (DFT)[11–13] have led to improved understanding of the same.

During the fabrication process, nanomaterials are subjected to chemical, thermal, and mechanical treatments that alter their surface morphology and hence their catalytic activity. A detailed study of the melting process of metal nanoclusters is useful in understanding their thermal stability.[7] The solid-liquid transition in nanoclusters differs significantly from that in bulk materials.[14,15] Both experimental and theoretical studies indicate that melting starts from the surface and propagates to the interior, with surface melting starting at temperatures significantly lower than the homogeneous transition temperature.[16–18] This phenomenon is a result of reduced coordination of surface sites compared to

bulk atoms, making them less constrained in their thermal motion. Melting at the nanoscale is known to proceed through an intermediate state at which solid and liquid states coexist (dynamic coexistence), and the structure fluctuates between solid and liquid.[19] Experimental studies and molecular simulations[9,20] give further insights into the dependence of the nanomaterial melting point on size, shape, and composition. In most cases, the cluster melting point is lower than bulk melting value, and is known to decrease with cluster size. The variation of melting point is not always a monotonically increasing function of cluster size, with quantum effects playing a role at smaller cluster sizes.[21–23]

Previous studies in catalysis and sensing applications have indicated improved selectivity towards specific reactions obtained by controlling surface composition of alloys.[24–26] The alloying process leads to variations in structure and surface atomic distribution depending on nanocluster size, shape, and overall composition. At the nanoscale, bimetallic nanoclusters exhibit a phenomenon known as surface segregation, in which one of the metals preferentially segregates to the surface. The relative surface energy difference between the two metals dictates the extent to which segregation occurs.[27,28] Additional complexities are induced by micromixing. As a result, the melting behavior of alloys differs significantly from that of single-component metal nanoclusters.

Supported bimetallic clusters are used extensively in catalysis and sensor applications, with the support used primarily to provide mechanical stability. The support also serves to spread out the metal cluster over more surface area. Recently, the bottom-up approach based on the concepts of self-organization and self-assembly of suitable nanostructures on a substrate is emerging as a viable alternative for low-cost manufacturing of nanostructured materials.[29] However, substrate-induced effects on nanoparticle properties are difficult to predict due to the lesser known nature of metal-substrate interactions.[30]

Model catalysis studies involve deposition of transition metal clusters in submonolayer quantities on a substrate, with the morphology and reactivity studied by surface sensitive techniques such as scanning tunneling microscopy (STM), thermal desorption spectroscopy and x-ray photoelectron spectroscopy.[29] It is expected that the substrate should mimic the properties of the support material used in real catalysis and sensing applications. However, the strong interaction of metal oxides such as TiO_2 and MgO with metal clusters makes it difficult to study experimentally.[30] An alternative is to use a relatively inert substrate such as graphite or gold so that the underlying properties of the cluster can be isolated from that of the substrate.[31] Graphite, which represents the most stable allotropic form of carbon, also has a relatively higher melting point compared to the nanoclusters under study. This makes it an excellent candidate for determining thermal characteristics of supported transition metal nanoclusters.

Highly oriented pyrolitic graphite substrates have been utilized to grow Pt nanoparticles using pulsed-laser deposition techniques.[32,33] Cluster atomic distributions characterized by STM have been used to gain insights into the growth kinetics. It is likely that the surface defects on the graphite substrate act as nucleation sites for the diffusing Pt species. Similarly, the properties of other metal clusters such as those of gold,[8,10] platinum,[34] and Cu-Ni (see Ref. 5) on a graphite substrate have been studied in the past and the metal-substrate interactions have been found to result in properties that are different from those of isolated clusters. Graphite-supported cubic and tetrahedral platinum nanocrystals of 8 nm diameter were found to evolve to spherical shapes at temperatures higher than 500 °C, with surface and total melting occurring at a slightly higher temperature.[35] Nanocluster diffusivity on surfaces plays a key role in cluster aggregation processes. Experimental studies suggest rapid diffusion of small antimony clusters on graphite substrates, a fact corroborated by molecular dynamics (MD) studies of Lennard-Jones (LJ) clusters diffusing on nonepitaxial crystalline surfaces.[36] Similar MD studies conducted on 249-atom gold nanoclusters indicated high diffusivity on graphite surface.[8] The role played by substrate atoms on the thermal stability and melting behavior of nanoclusters have been studied only to a limited extent. A comprehensive understanding of the structure and dynamics of substrate-supported metal nanoclusters and their effect on the melting behavior of bimetallics is desirable.

In most experimental studies, melting is characterized by changes in shape. However, shape changes are also observed when solid nanoparticles on a substrate jump from one local minimum to another, making it difficult to calculate the precise transition temperature.[7,37] Experimental studies to understand the role played by a substrate on nanocluster properties are both cost intensive and are sometimes difficult to perform. MD simulations offer a simple and comprehensive tool to understand the complex microscopic phenomena of segregation and micromixing, and provide insights into the role played by the substrate. In the present work, we employ MD simulations to study the properties of Pd-Cu, Pd-Rh, and Pd-Pt nanoclusters of varying compositions and sizes, supported on a graphite substrate. The large available experimental data on graphite supported nanoclusters as well as the recent advances in experimental techniques[29] can help provide insights into the validity of the simulation results.

II. INITIAL CONFIGURATION SETUP

All the transition metals under study in this work (Cu, Pd, Pt, and Rh) have an fcc structure. Hence, an fcc block/lattice of 500 atoms was constructed from an fcc unit cell by replication in the *ABC* direction with the center located at (0, 0, 0). The initial atomic positions of the bimetallic system were determined using Metropolis Monte Carlo simulations employing the bond order simulation (BOS) model.[27,28] The energy parameters and site energies needed for the BOS model were generated using DFT by Yang,[38] and the same values have been used in the present study. This approximately cubic nanocluster is supported on a graphite substrate, with the initial metal-substrate distance set to 2 Å. The graphite substrate containing 3600 atoms in two layers was built by *AB* type stacking to have $73.8 \times 73.8 \times 6.7$ Å^3 dimensions. The surface segregation phenomenon present in bimetallic nanoclusters results in lower surface energy atoms being located

at low coordination number sites such as surfaces, edges, and corners. The extent of surface segregation depends on a number of factors, such as difference in surface energy, mixing energy, and entropy. The final microstructure is a result of interplay among these factors.[27,28] In the present case, the segregation profile of Pd atoms is different in the three bimetallics (Pd-Cu, Pd-Pt, and Pd-Rh). In case of Pd-Cu, Cu with much lower surface energy completely segregates to the surface, with Pd atoms forming the cluster core. The reverse is true for Pd-Rh, where Pd has much lower surface energy than Rh. Pd-Pt represents an intermediate case with more Pd atoms located at the surface than Pt, due to slightly lower surface energy of Pd than that of Pt.

III. COMPUTATIONAL DETAILS

A. Pair potential function

MD simulations were performed using DL_POLY[39] to gain insights into the melting process at the atomistic level. The embedded atom potential[40] and other long range potentials like the Sutton-Chen potential[41] based on Finnis-Sinclair type of potentials have been used in the literature successfully to predict the properties of fcc-based metals such as Pd, Cu, Rh, and Pt. The local electronic density is included to account for the many-body terms.

Based on the Sutton-Chen model, the potential energy of the finite system is given by

$$U_{tot} = \sum_i U_i = \sum_i \varepsilon \left[\sum_{j \neq i} \frac{1}{2} V(r_{ij}) - c\rho_i^{1/2} \right]. \quad (3.1)$$

Here, $V(r_{ij})$ is a pair potential to account for the repulsion resulting from Pauli's exclusion principle:

$$V(r_{ij}) = \left(\frac{a}{r_{ij}} \right)^n. \quad (3.2)$$

The local electronic density accounting for cohesion associated with any atom i is given by

$$\rho_i = \sum_{j \neq i} \phi(r_{ij}) = \sum_{j \neq i} \left(\frac{a}{r_{ij}} \right)^m. \quad (3.3)$$

The Sutton-Chen potential predicts properties involving defects, surfaces, and interfaces poorly. The quantum Sutton-Chen potential[42] (hereafter referred to as QSC), includes quantum corrections and takes into account the zero point energy, allowing better prediction of temperature-dependent properties. The QSC potential function was found to be better suited to melting and phase transformation studies of bulk Cu-Ni and Cu-Au alloys.[43,44] The QSC parameters for the metal atoms are listed in Table I. The geometric mean was used to obtain the energy parameter ε and the arithmetic mean was used for the remaining parameters, to model the nature of interaction between metal atoms.

To represent the relatively weak interactions between the carbon atoms in the graphite substrate and an adsorbed metal atom, the LJ potential function has been used. Previous work on substrate supported metal nanoclusters indicates that the LJ potential for this interaction provides reasonable predictions of the thermal behavior of the clusters.[5] The LJ parameters ($\varepsilon = 0.002\,413$ eV, $\sigma = 3.4$ A) for graphite have already been determined in studies of small-molecule physisorption, to quantitatively describe properties such as monolayer structure and phase transitions.[45–48] The LJ parameters for metal atoms were taken from Agrawal[49] and Lorentz-Berthelot mixing rules were employed to find well-depth and size parameters for metal-C interactions. These parameters are listed in Table II. A static substrate with fixed positions for C atoms was used to reduce the computational load.

TABLE I. Potential parameters used in MD simulations for metal-metal interactions.

Quantum Sutton-Chen	n	m	ε (eV)	c	a (Å)
Pd	12	6	3.2864×10^{-3}	148.205	3.8813
Pt	11	7	9.7894×10^{-3}	71.336	3.9163
Rh	13	5	2.4612×10^{-3}	305.499	3.7981
Cu	10	5	5.7921×10^{-3}	84.843	3.603

B. MD simulation details

The MD simulations were carried out in an ensemble approximating the canonical with a constant number of atoms N and volume V (much larger than the cluster size) without any periodic boundary conditions. A constant-temperature Berendson thermostat with a relaxation time of 0.4 ps was used. The equations of motion were integrated using the Verlet leapfrog algorithm[50] with a time step of 0.001 ps. The nanocluster was initially subjected to mild annealing in the 0–300 K interval. This was followed by heating to 1800 K in increments of 100 K. Near the melting point, the temperature increments were reduced to 10 K to account for the large temperature fluctuations. The simulations were carried out for 400 ps of equilibration followed by a production time of 200 ps for generating time-averaged properties.

IV. RESULTS AND DISCUSSION

The following subsections discuss identification of the nanocluster melting point and characterization of structural changes associated with the melting phenomenon for the three bimetallics at the 50% Pd representative composition. Particular emphasis is on Pd-Cu and Pd-Rh nanocluster which have contrasting segregation profiles for Pd. Dynamic

TABLE II. Potential parameters used in MD simulations for metal-graphite interactions.

LJ potentials	ε (eV)	σ (Å)
Pd-C	0.033 5	2.926
Pt-C	0.040 92	2.936
Rh-C	0.040 72	2.898
Cu-C	0.031 64	2.839

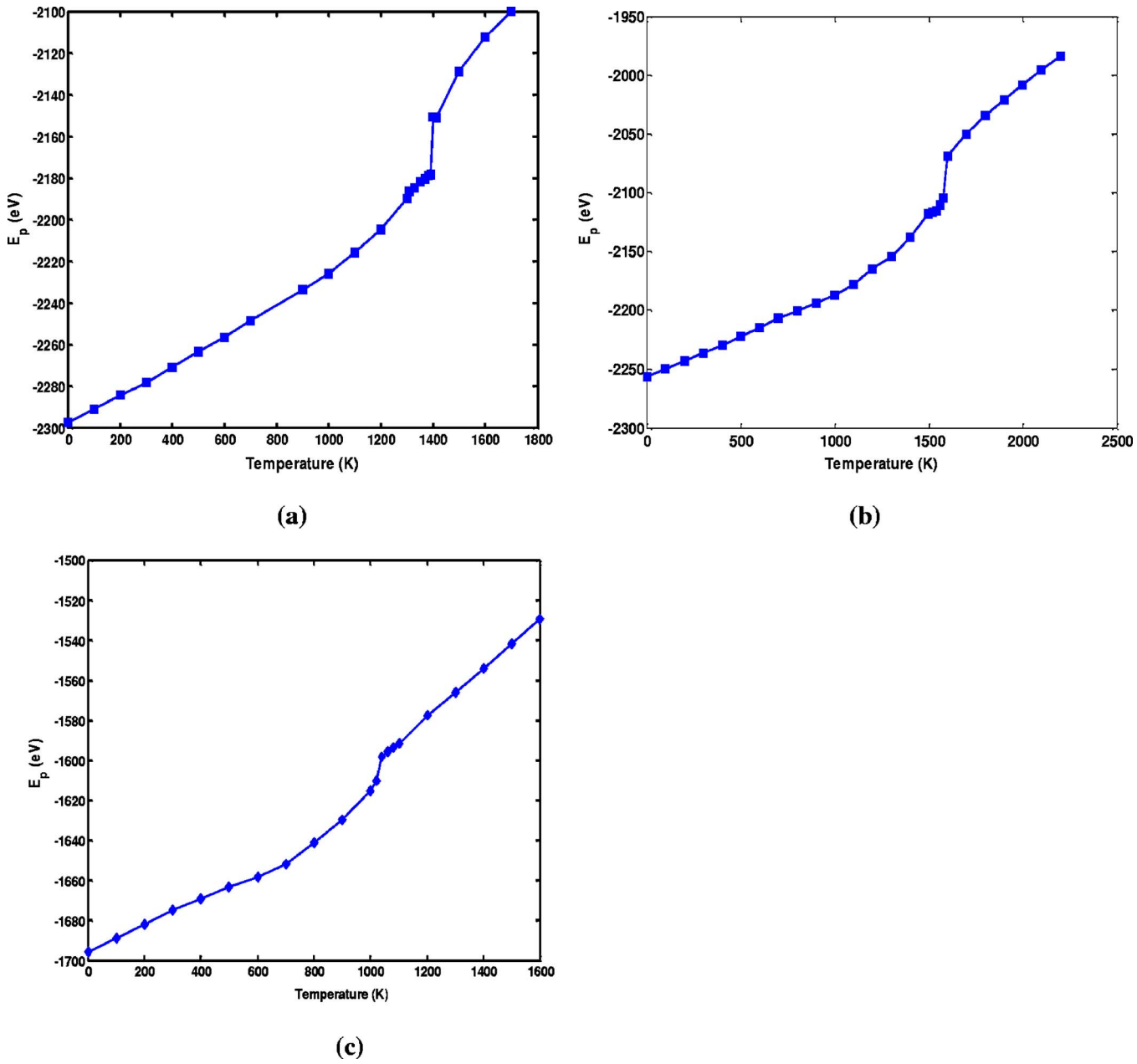

FIG. 1. (Color online) Potential energy variation with temperature for $(Pd_{0.5}\text{-}X_{0.5})_{500}$ clusters (a) X=Pt (b) X=Rh (c) X=Cu.

properties through the nanocluster melting process and the effect of varying compositions of bimetallics on the thermal characteristics are studied and discussed. The effect of graphite support on the cluster diffusivity and melting properties is also investigated.

A. Melting point identification

The transition temperature from solid to liquid phase is usually identified from the variation in either the thermodynamic properties such as potential energy and specific heat capacity or structural properties such as bond orientational order parameters or Wigner values. The present study employs both these methods to identify melting points for different cluster sizes and compositions.

1. Potential energy

Figure 1 shows the temperature dependence of the overall potential energy for the $(Pd_{0.5}-X_{0.5})_{500}$ atom clusters, where X=Pt, Rh, or Cu. The potential energy shown in Fig. 1 includes both the metal-substrate interactions as well as the metal-metal interaction. Our calculations indicate that the contribution of the metal-substrate interaction to the overall potential energy is at least two orders of magnitude less than that of metal-metal interaction for all the three clusters.

The transition from a solid to a liquid phase can be identified by a simple jump in the total potential energy curve. This corresponds to a melting temperature of 1390±10 K for $(Pd_{0.5}\text{-}Pt_{0.5})_{500}$, 1590 K±10 K for $(Pd_{0.5}\text{-}Rh_{0.5})_{500}$ and 1020±10 K for $(Pd_{0.5}\text{-}Cu_{0.5})_{500}$, as seen in Fig. 1. We find

that at temperatures greater than 800 K for Pd-Pt, 900 K for Pd-Rh, and 600 K for Pd-Cu, the metal-graphite energy decreases with temperature and undergoes a sudden decrease near the melting point. The small decrease could be attributed to the increased metal-substrate interaction resulting from the collapse of the solid structure at the melting point. The metal-metal interaction, on the other hand, increases with temperature. Positive deviations from linearity in the metal-metal potential energy curve indicate the tendency of the clusters to surface melt. The metal-substrate energy profile follows an opposing trend in the temperature range where surface melting occurs. Therefore, the metal-substrate interaction tends to delay the onset as well as to reduce the extent of surface melting in nanoclusters, thereby resulting in a delay in the final solid-liquid phase transition.

The variation of total potential energy with temperature for clusters of different compositions is discussed in subsequent sections. These melting temperatures are 100–200 K higher than those for isolated clusters of similar composition and size. Numerical comparison of the melting transition temperatures is provided later in this paper. The delay in the onset of the melting point is a result of the lesser degree of freedom for atoms close to the substrate. Influence of the graphite support on the dynamics of cluster melting will be discussed in subsequent sections.

2. Specific-heat capacity

The specific-heat capacity (C_v) in a weak coupling ensemble such as achieved with the Berendson thermostat can be written as a function of fluctuations in the potential energy $\langle(\delta E_p)^2\rangle$.[51] Strictly speaking, the specific-heat capacity also includes the contribution arising from the ideal gas kinetic energy, which is, however, constant, and hence has no effect on the change of C_v with temperature:

$$C_v = \frac{k\langle(\delta E_p)^2\rangle}{(kT)^2 - 2\alpha\langle(\delta E_p)^2\rangle/3N}, \tag{4.1}$$

where $\langle(\delta E_p)^2\rangle = \langle E_p^2\rangle - \langle E_p\rangle^2$ and α is the ratio of the standard deviations of kinetic and potential energies:

$$\alpha = \sqrt{\langle(\delta E_k)^2\rangle/\langle(\delta E_p)^2\rangle}. \tag{4.2}$$

Morishita has proved that a weak coupling ensemble approaches a canonical ensemble for very short relaxation times ($\alpha \approx 0$) and to a microcanonical ensemble for longer relaxation times ($\alpha \approx 1$). In the present case, the Berendson thermostat with a coupling parameter of 0.4 ps leads to $\alpha \approx 10^{-4}$, making the calculation for specific-heat capacity similar to that of a canonical ensemble as given in Eq. (4.3):

$$C_v = \frac{k\langle(\delta E_p)^2\rangle}{(kT)^2}. \tag{4.3}$$

To identify the melting temperature, the specific-heat capacity at constant volume is plotted in Fig. 2. For all three $(Pd_{0.5}\text{-}X_{0.5})_{500}$ clusters, the maximum in the specific-heat capacity corresponds to the temperature where a jump in potential energy is observed. This leads to melting temperature estimates of $T_m = 1390 \pm 10$ K, $1590\ \text{K} \pm 10$ K, and 1020 ± 10 K for $(Pd_{0.5}\text{-}Pt_{0.5})_{500}$, $(Pd_{0.5}\text{-}Rh_{0.5})_{500}$, and $(Pd_{0.5}\text{-}Cu_{0.5})_{500}$, respectively. Our calculations reveal that the metal-substrate part has little effect on the specific-heat capacity of the clusters. The specific-heat capacity calculated on the basis of the fluctuations in the metal-substrate energy identifies same transitions as those shown in Fig. 2. However, they are an order of magnitude smaller than those reported in Fig. 2.

The small peaks in the specific-heat capacity curve at temperatures lower than the actual melting point indicate onset of surface melting. The early onset of surface melting at about 500 K in case of Pd-Cu would mean that the extent of surface melting is much more than in Pd-Pt and Pd-Rh. Indeed, experimentally based interfacial energies and crystallographic considerations suggest Cu and Pd nanoclusters to surface melt a lot more than Pt and Rh.[52,53]

3. Bond orientational order parameters

There are several criteria used to identify local and extended orientational symmetries. One such method is the bond orientational order parameter (BOP) method,[54] which is used to analyze cluster structure as well as to distinguish between atoms in solid (closed packed) and liquid environment generated at the onset of melting. The value of the global bond orientational order parameter Q_l in a solid cluster depends on the relative bond orientations and has a unique value for each crystal structure. Based on local solid symmetry, it was found that cubic and decahedral clusters have nonzero values of $q_l(i)$ for $l \geqslant 4$ and at $l=6$ for those with icosahedral symmetry. All global order parameters vanish in isotropic liquids for $l > 0$. The global bond orientational order values for different types of symmetry are reported in Table III.

The atoms in a solid undergo vibrations about their equilibrium positions, leading to distortion of the crystal structure that is characterized by Q_4 and Q_6 values. The magnitude of the nonzero $\{Q_l\}$ values depends on the definition of nearest neighbors and can be changed by including surface bonds in the average. The cutoff distance (r_{cut}) for identifying the nearest neighbors was taken to be 3.6 A at 300 K. This corresponds to the position of the first minimum in the pair correlation function for fcc Pd-Pt. The cutoff distance (r_{cut}) at other temperatures and different clusters were similarly identified.

Figure 3 shows the variation in BOP with temperature for the three bimetallics. Comparison of Q_4 and Q_6 values for fcc with those in Fig. 3 indicates rapid structural rearrangement in all three bimetallic nanoclusters when subjected to annealing between 0 and 300 K. The change in order parameters of Pd-Cu is more continuous than in the cases of Pd-Rh and Pd-Pt. The rapid structural changes in the Pd-Cu might be attributed to the early onset as well as to the greater extent of surface melting. Figures 3(a) and 3(b) indicate Pd-Rh to surface melt more in comparison to Pd-Pt. This effect is more pronounced with increasing compositions of Cu in Pd-Cu and Pd in Pd-Pt and Pd-Rh. These

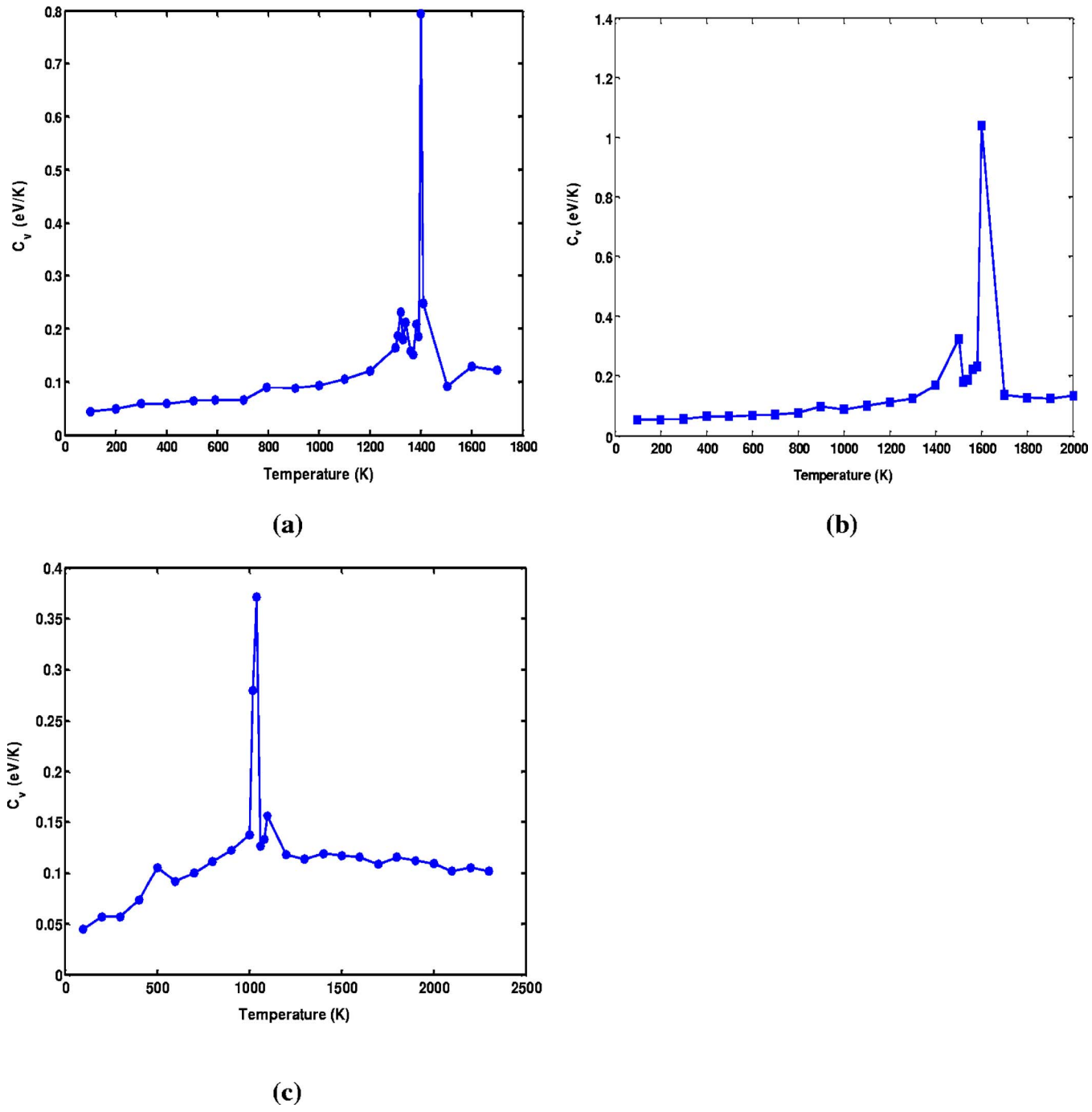

FIG. 2. (Color online) Variation of specific-heat capacity with temperature for $(Pd_{0.5}-X_{0.5})_{500}$ clusters (a) X=Pt (b) X=Rh (c) X=Cu.

observations are in line with the experimental studies that suggest a surface melting order of Cu>Pt>Rh.[37] All the three nanoclusters show a transformation to a more-or-less hcp structure before the melting transition. At the melting point, the Q_4 order parameters of all the three nanoclusters show a sudden decrease to near zero, indicating the transition from solid to liquid phase. The global order parameter Q_6 for the three clusters has nonzero values after the phase transition, which could be attributed to the layering effect of the substrate. The melting points found using these order parameters match those found using potential energy and specific-heat capacity curves.

TABLE III. Bond orientational order parameter values for various geometries.

Geometry	Q_4	Q_6
fcc	0.190 94	0.574 52
hcp	0.097 22	0.484 76
bcc	0.036 37	0.510 69
Icosahedral	0	0.663 32
sc	0.763 76	0.353 55
Liquid	0	0

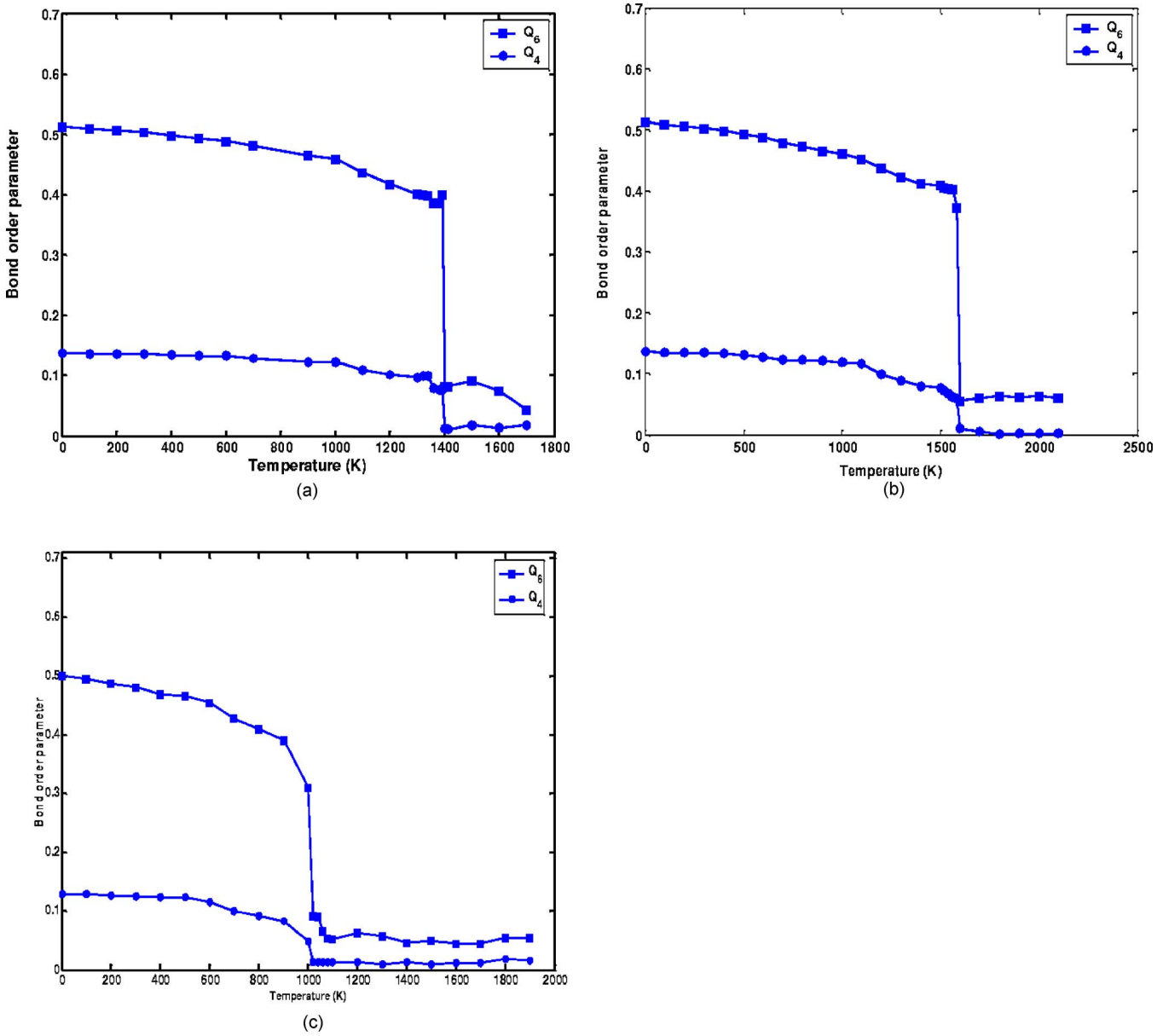

FIG. 3. (Color online) Variation of bond orientational order parameters with temperature for $(Pd_{0.5}-X_{0.5})_{500}$ clusters (a) X=Pt (b) X=Rh (c) X=Cu.

B. Structure and dynamics of cluster melting

The following subsections discuss the structural and dynamical changes associated with cluster melting. Influence of the graphite field on these properties is also discussed, as is the effect of composition.

1. Analysis of density profiles

Figure 4 shows the atomic distributions of Cu and Pd atoms, respectively, during the melting process for the $(Pd_{0.5}\text{-}Cu_{0.5})_{500}$ cluster along the z-axis, perpendicular to the surface. Sharp peaks in the density distributions of both Cu and Pd are evident below the melting transition temperature. The sharper peaks for Pd than for Cu at 900 K, a little below the melting temperature, are possibly indicative of higher mobility of Cu atoms. This conclusion is strengthened by other properties that indicate surface melting, and surface segregation of Cu atoms. The distributions for both Pd and Cu at 1020 and 1030 K (slightly above the melting transition temperature) indicate that the weak graphite field is able to structure both Cu and Pd in the first few monolayers. This layered structuring in the first few monolayers is evident even at the much higher temperature of 2000 K, for both Cu and Pd. It appears that the bimetallic cluster can wet the graphite surface, and the observed layering effects from the graphite substrate (for clusters) are a result of the finite time of simulation. The effect of a change in the cluster composition is manifested in the form of structural changes as a function of temperature. There is higher Cu enrichment near the graphite substrate with increasing Cu composition in the bimetallic.

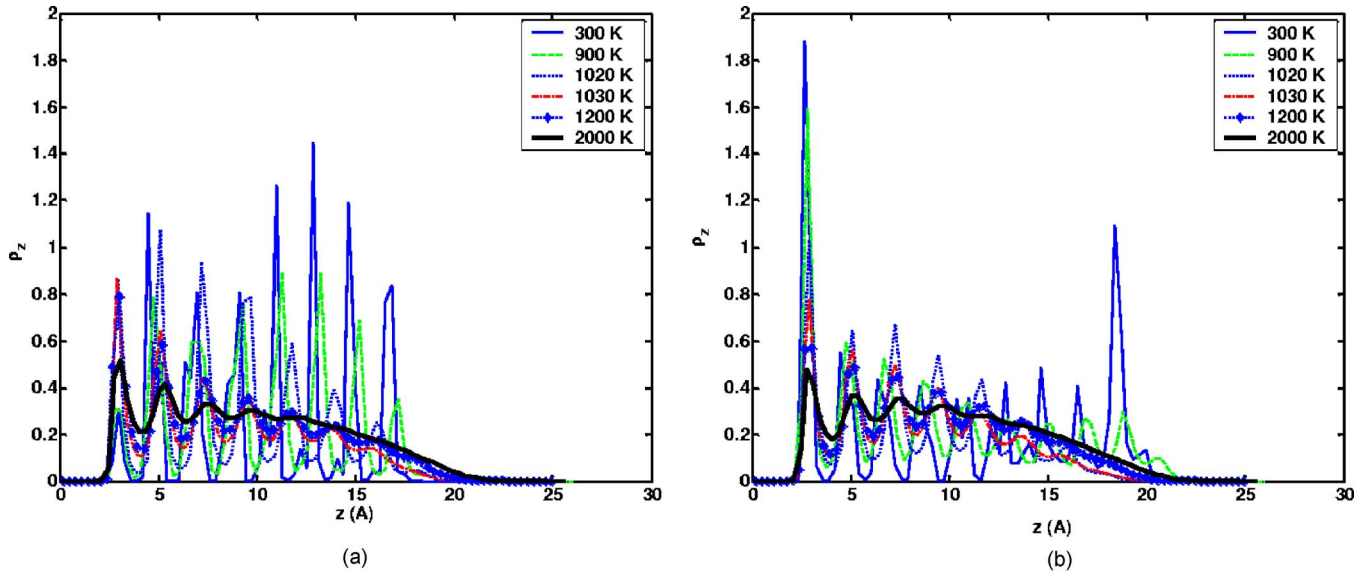

FIG. 4. (Color online) Density profile representing number density (number of atoms/volume) of atoms as a function of temperature for (a) Pd and (b) Cu from simulations of the $(Pd_{0.5}\text{-}Cu_{0.5})_{500}$ cluster.

Similar wetting features are observed in the cases of $(Pd_{0.5}\text{-}Rh_{0.5})_{500}$ and $(Pd_{0.5}\text{-}Pt_{0.5})_{500}$. In both these cases, Pd with lower surface energy enriches the surface. In both cases of Pd-Pt and Pd-Rh clusters, Pd with smaller LJ well depth tends to wet the graphite substrate more. Even though C-Rh and C-Pt LJ well depth parameters are larger than that of C-Pd, leading one to expect Rh and Pt to be present at the surface more, it is the higher cohesive energy (higher melting point) resulting from stronger Rh-Rh and Pt-Pt interactions, which leads to Pd spreading on the graphite substrate and Rh and Pt retaining their hemispherical shape. This is shown for Pd-Rh in Fig. 5. As the percentage of Pd in the bimetallic increases, the Pd wetting phenomenon also increases. The delicate balance between the metal-metal and metal-graphite interactions determines these wetting characteristics.

2. Deformation parameters

To explore the surface melting behavior and the associated shape changes, we use deformation parameters.[55] and shell-based self-diffusion coefficients.[55]

The melting phenomenon is associated with changes in nanocluster size and shape resulting from the relative diffusion of Cu and Pd atoms. To characterize these transformations, we use deformation parameters given by

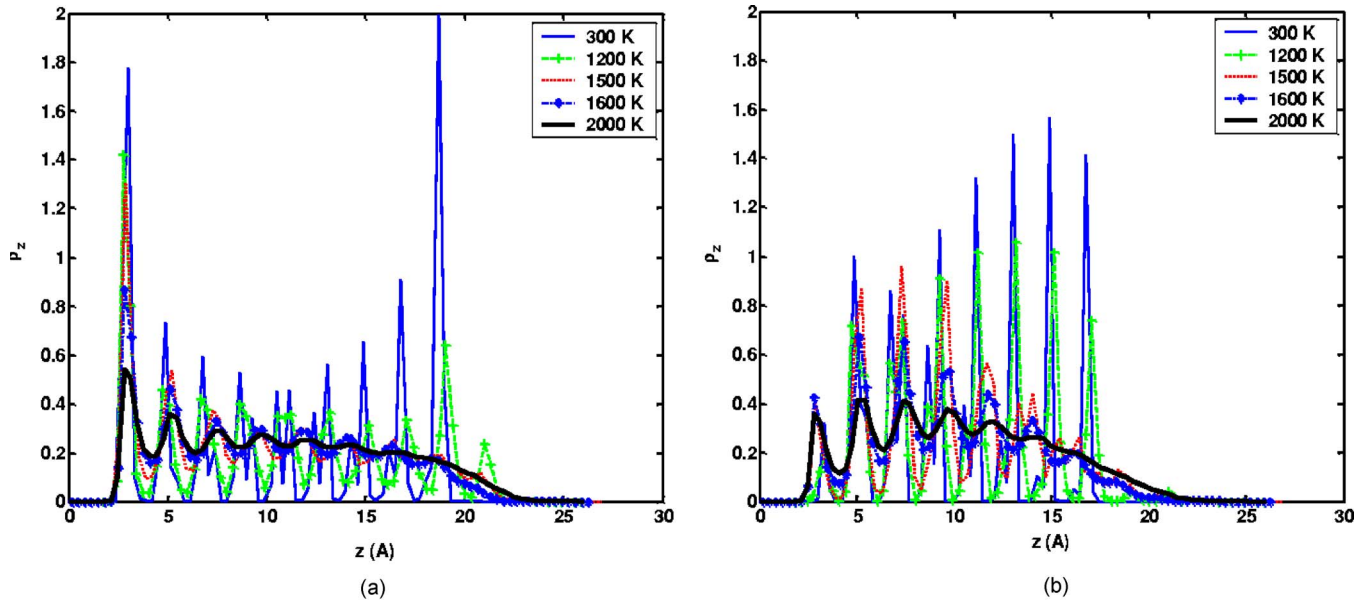

FIG. 5. (Color online) Density profile representing number density (number of atoms/volume) of atoms as a function of temperature for (a) Pd, (b) Rh from simulations of the $(Pd_{0.5}\text{-}Rh_{0.5})_{500}$ cluster.

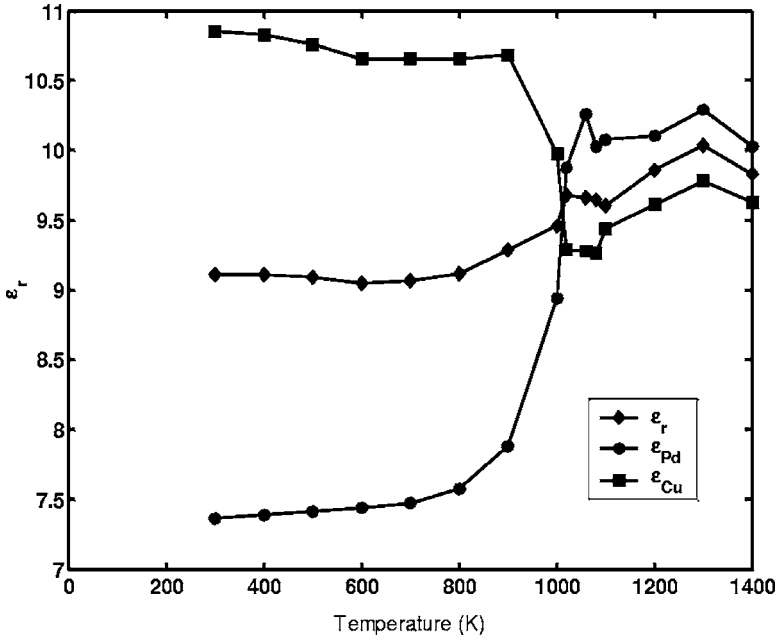

FIG. 6. Deformation parameter for $(Pd_{0.5}\text{-}Cu_{0.5})_{500}$ at different temperatures.

$$\varepsilon_q = \frac{\sum_{i=1}^{N} |q_i - q_{cen}|}{N}, \tag{4.4}$$

where q_i refer to either the position coordinates of the ith atom in an N-atom cluster along one of the three (x,y,z) directions, or the position vector $\mathbf{r}(x,y,z)$, and q_{cen} is the cluster center of mass.

Figure 6 shows the deformation parameters for $(Pd_{0.5}\text{-}Cu_{0.5})_{500}$ plotted as functions of temperature. Equation (4.8) indicates atoms with larger deformation parameter to be located farther from the cluster center of mass. As $\varepsilon_{Cu} > \varepsilon_{Pd}$ at low temperatures, the initial cluster structure is segregated with Cu atoms located at surface and cluster-core composed of Pd. Near the phase transition, ε_{Cu} decreases, whereas ε_{Pd} increases indicative of the inward diffusion of the Cu atoms and outward diffusion of Pd atoms, thereby leading to a change in the overall cluster structure. In addition, the atomic composition at the metal-graphite interface changes, thereby affecting the cluster diffusivity on the graphite substrate. Similar behavior is observed for Pd-Rh and Pd-Pt clusters where Pd atoms move to the interior and Rh (in Pd-Rh), Pt (in Pd-Pt) to the outside.

3. Diffusion coefficients

The cluster diffusion coefficient is given by

$$D = \frac{1}{6\Delta t}\langle |[r_i(t+k) - r_i(k)]|^2 \rangle, \tag{4.5}$$

where $r_i(t)$ represents vector position of the ith atom at time t with averages taken over k time origins.

As indicated in our earlier work,[55] better insights into the surface melting process can be obtained by calculating shell-based diffusion coefficients. In the present case, insights into the effect of graphite field on the melting of different layers in nanocluster could be studied by partitioning the cluster into shells of equal width (dz) in a direction (z) perpendicular to the graphite substrate. Mean-square displacements calculated within each shell were used to calculate the self-diffusion coefficients using Eq. (4.9) for atoms in that shell. The average interatomic distance between atoms in the bimetallic was used as dz. This corresponds to 2.66, 2.75, and 2.72 Å for Pd-Cu, Pd-Pt, and Pd-Rh, respectively. The atoms were assigned to the bins (shells) based on their initial positions at the end of the equilibration period. The mean square displacements for each shell were then generated by averaging over a 200 ps trajectory with sampling done every 0.1 ps.

As seen in Fig. 7(b), at low temperatures (300–500 K), the diffusion coefficients of different shells are nearly the same. However, as temperature increases to 600 K, the outermost shells (7 and 8) with the majority of atoms located far away from the graphite substrate, show relatively higher diffusivity. Melting clearly starts from the cluster surface. However, in the case of supported clusters, it starts from the surface which experiences the least influence of the graphite field. This is evident from the much higher diffusivity of shell 8 located farthest (~19.75 Å) from the graphite substrate. With further increase in temperature (800–900 K), the effect of the graphite substrate is confined to a few monolayers and more shells (5–8) exhibit the same behavior. Above the melting point, all the shells show relatively greater diffusivity indicative of phase transformation. Cluster snapshots taken at different temperatures corroborate the same (Fig. 8). Interestingly, the layer (shell 1) closest to the graphite substrate exhibits much higher diffusivity compared to second, third, and fourth shells at 900 K for this Pd-Cu cluster. This effect could be a result of increased number of Cu atoms having higher diffusivity than Pd, in shell 1 at elevated temperatures [Fig. 8(e)], thereby signaling the onset of surface melting in this layer.

Similar surface melting features are observed in cases $(Pd_{0.5}\text{-}Pt_{0.5})_{500}$ and $(Pd_{0.5}\text{-}Rh_{0.5})_{500}$, although the onset of

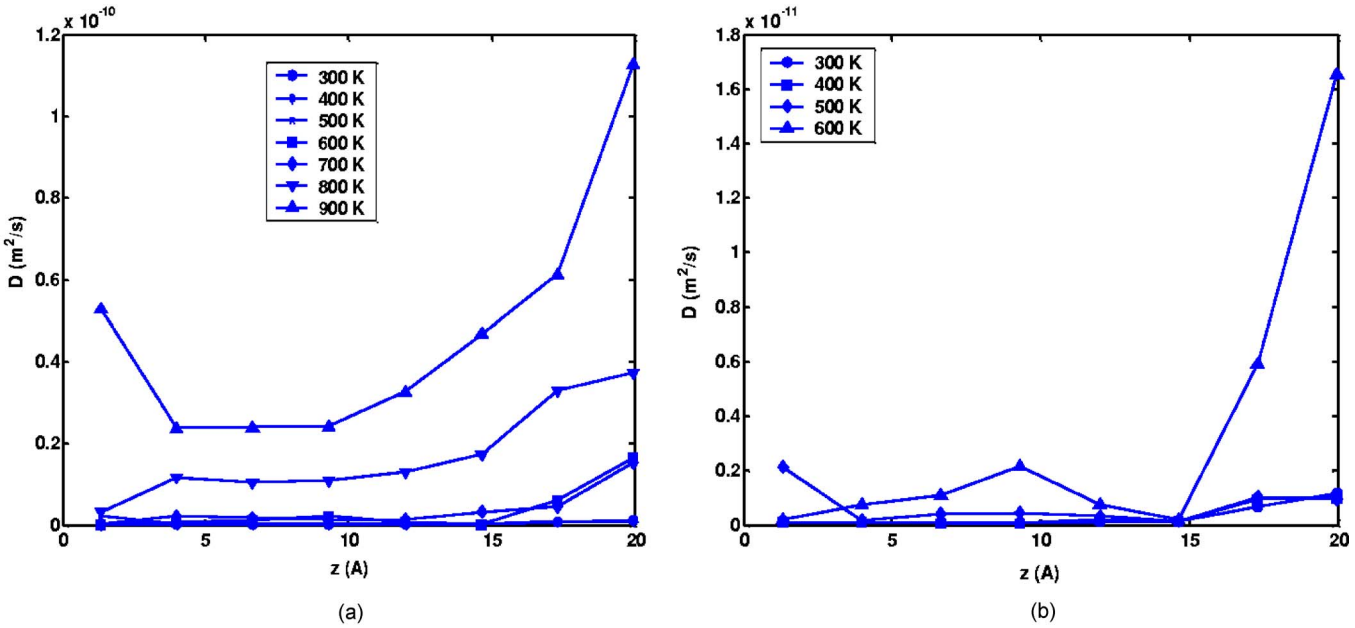

FIG. 7. (Color online) Shell based diffusion coefficients in z-direction for $(Pd_{0.5}\text{-}Cu_{0.5})_{500}$ at (a) Temperatures leading up to melting (300–900 K) (b) Low temperatures (300–600 K).

surface melting takes place at slightly higher temperatures. Same-sized clusters richer in Pd (in case of Pd-Rh and Pd-Pt) and Cu (in case of Pd-Cu) compositions surface-melt more in comparison to others.

4. Velocity autocorrelation functions

Figure 9 shows normalized in-plane $[\Psi_r=\langle V_r(t_k)\cdot V_r(t_k+t)\rangle]$ and out-of-plane $[\Psi_z=\langle V_z(t_k)\cdot V_z(t_k+t)\rangle]$ velocity auto-

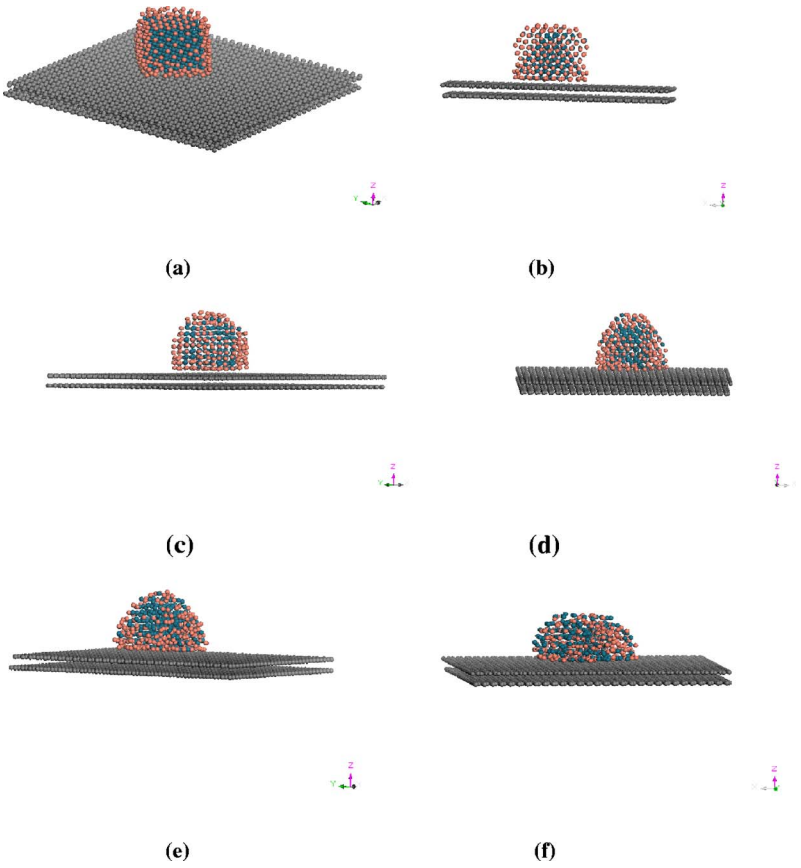

FIG. 8. (Color online) Cluster snapshots taken at different temperatures for $(Pd_{0.5}\text{-}Cu_{0.5})_{500}$ at (a) 300 K, (b) 500 K, (c) 600 K, (d) 700 K, (e) 900 K, and (f) 1000 K.

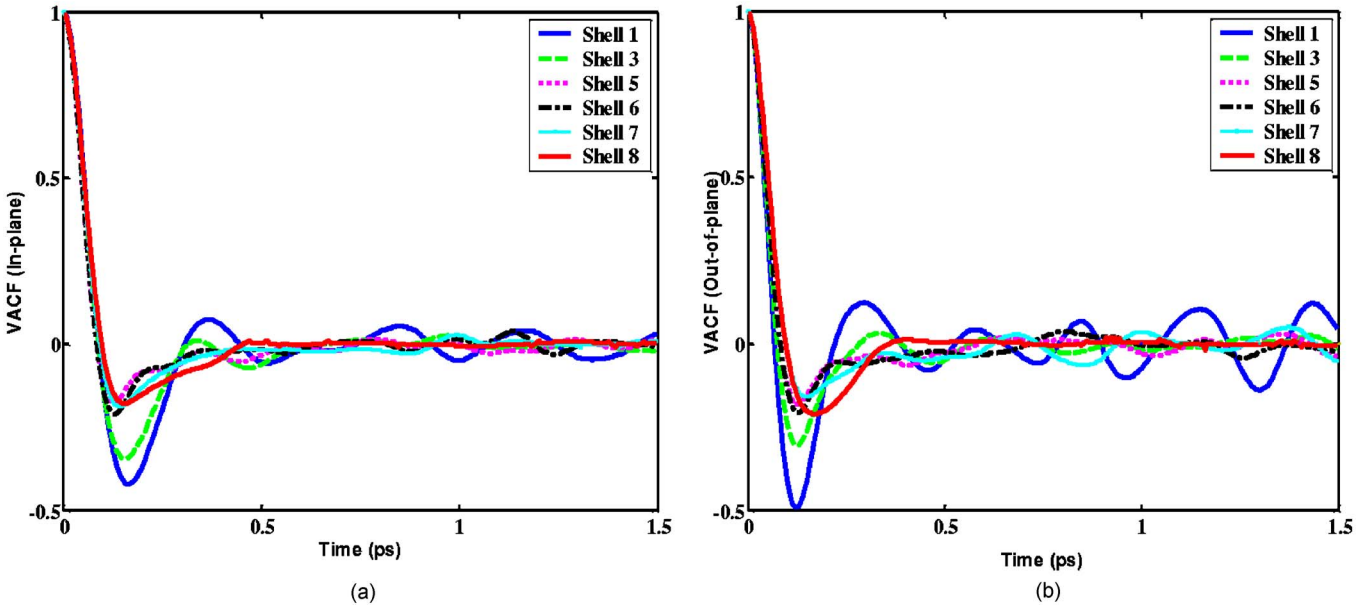

FIG. 9. (Color online) Shell based velocity autocorrelation function for Cu atoms in $(Pd_{0.5}\text{-}Cu_{0.5})_{500}$ at 900 K. (a) In-plane. (b) Out of plane.

correlation functions (Ψ) calculated for Cu and Pd atoms for different shells along the z-direction perpendicular to the graphite substrate at 900 K. The partitioning of shells has been discussed in the previous section and few shells are omitted in Fig. 9 for clarity. At high densities (solid phase), atoms are closely packed, causing rebounding oscillations to be more numerous than scattering collisions, and many rebounds cause Ψ to change sign. At lower densities within the cluster corresponding to the liquid phase, $\Psi(t)$ becomes negative and passes through a minimum before approaching zero. The above arguments and Figs. 9(a) and 9(b) suggest shells 1–3 (closer to graphite substrate) to exhibit solid-like and those far away (shells 5–8) to exhibit liquid-like characteristics for Cu atoms. Similarly, Pd atoms in shells 1–7 exhibit solid-like characteristics and those in 8 show liquid-like behavior. This suggests surface melting to start from the surface that experiences the least influence of the graphite field.

Components of velocity autocorrelation function (Ψ_r and Ψ_z) characterize the diffusion of Cu and Pd atoms at 900 K in the x-y plane (in plane) and z-direction (out of plane), respectively. Comparison of Ψr [Fig. 9(a)] and Ψ_z [Fig. 9(b)] for Cu atoms, indicate shorter correlation time and much larger depth of minima for the latter signifying larger z-directional motion than in the x-y plane. The greater z-directional motion is attributed to the stronger attractive pull of the graphite field on the surface-melted Cu atoms. Similar diffusion characteristics (larger z-directional motion) are also observed for Pd atoms in all shells, with most of the shells (1–7) exhibiting solid like characteristics as evident from the much higher rebounding oscillations. We find that Pd atoms in the outermost shell (shell 8) experience less attractive pull from the graphite field than Cu atoms in the same shell. The above arguments not only corroborate the results presented in the earlier sections, but also suggest peeling off of the surface- melted Cu atoms (as was evident from z-density profiles in Figs. 4 and 5, and the snapshots in Fig. 8), thereby exposing the inner solid Pd atoms (1–7). This effect becomes more profound with increasing compositions of Cu in Pd-Cu. The implications of such an exposure of Pd atoms on sensing applications would be discussed in subsequent sections. At still higher temperatures leading up to melting, even the shells closer to graphite substrate exhibit more scattering collisions than the rebounding oscillations suggesting a phase transformation to liquid.

In case of $(Pd_{0.5}\text{-}Pt_{0.5})_{500}$ and $(Pd_{0.5}\text{-}Rh_{0.5})_{500}$ nanoclusters, stronger metal-metal interaction results in similar behavior being observed at elevated temperatures; i.e., 1300 K and 1450 K, respectively. An increase in the composition of Pd in these nanoclusters results in a pronounced surface melting effect, leading to greater attractive pull on the surface melted atoms by the graphite field. The increased surface melting causes the otherwise weak graphite field to overcome the strong metal-metal interaction resulting in higher concentration of surface melted atoms (Cu in Pd-Cu, Pd in Pd-Pt and Pd-Rh) in shells closer to graphite substrate. Thus, the delicate balance between various metal-metal and metal-graphite interactions dictate the onset of surface melting as well as the diffusion characteristics (greater out of plane z-directional motion) of nanoclusters.

C. Effect of cluster composition on cluster melting point

Figure 10(a) shows the variation of melting point with composition for Pd-Pt clusters. The melting point of supported clusters is greater than unsupported clusters for all compositions. The reduced degrees of freedom of supported cluster atoms are responsible for the larger melting temperatures. While unsupported clusters exhibit a near-linear variation in melting point with composition, the supported clusters show a deviation from linearity for high Pd compositions. The near-linear variation for unsupported clusters results from the balance between the extent of surface

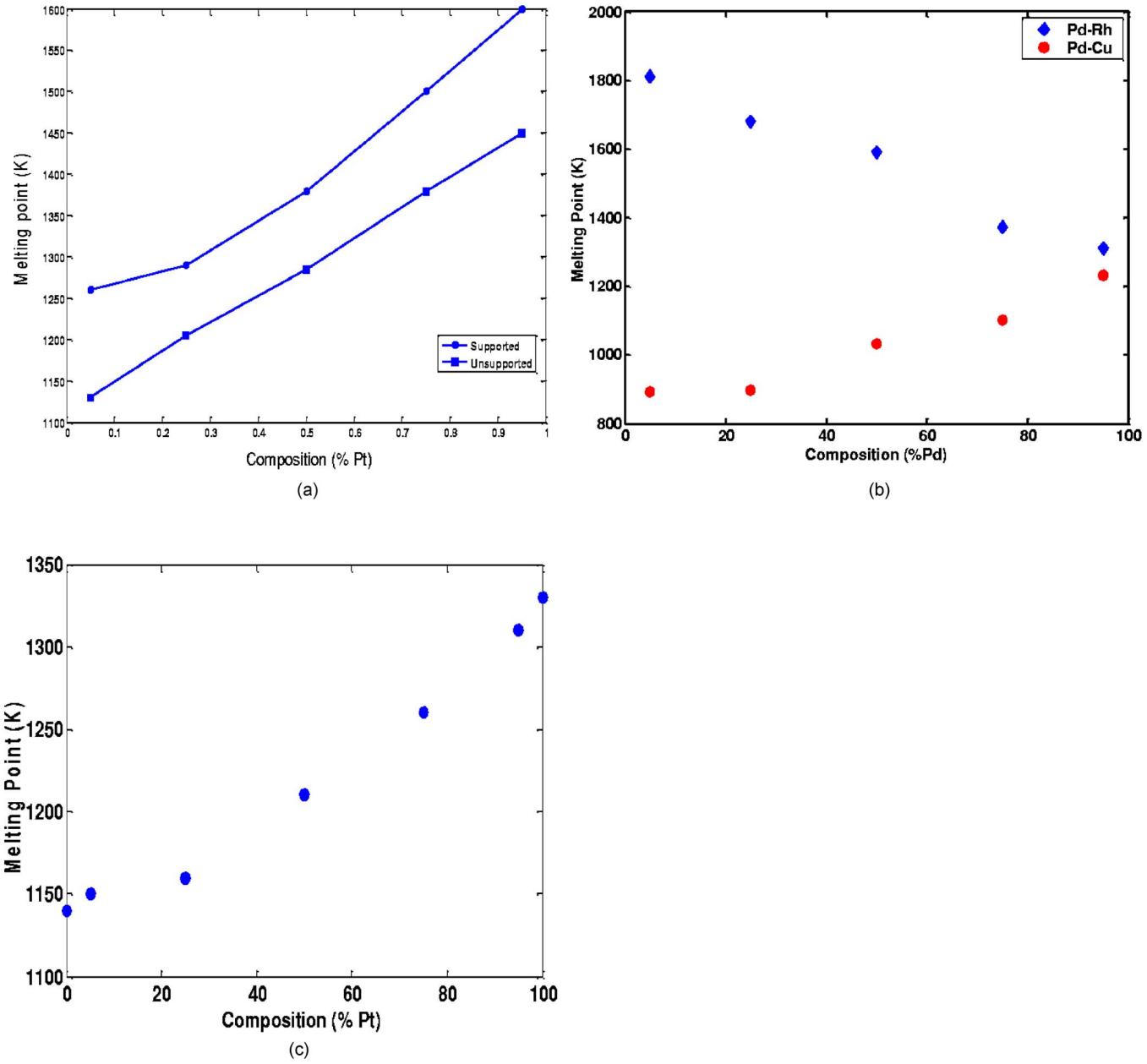

FIG. 10. (Color online) Variation of melting point with cluster composition for (a) supported and unsupported Pd-Pt clusters having 500 atoms, (b) supported Pd-Cu and Pd-Rh clusters having 500 atoms, and (c) supported Pd-Pt cluster having 256 atoms.

melting and the radius of the remaining solid core. At higher Pd compositions, reduced surface melting due to the effect of graphite field leads to nonlinear variation. In the cases of Pd-Cu and Pd-Rh nanoclusters [Fig. 10(b)], increasing compositions of Pd lead to an increase and decrease in melting points, respectively. However, in both cases, clusters rich in more surface-melting metals (Cu in Pd-Cu and Pd in Pd-Rh) exhibit much higher deviation from an otherwise linear behavior.

The finite size of nanocluster alloys leads to phenomena such as surface segregation, as well as surface melting, which results in the phase diagram of nanocluster alloys being different from those of bulk alloys. It is interesting to note from Fig. 10(a) that the difference between the melting points of pure Pd and Pt clusters correspond to 350 and 310 K for supported and unsupported cases, respectively. This is very close to the difference between bulk melting points for Pd and Pt calculated using the same potential function (330 K).[55] For small-cluster systems, it is expected that the melting point difference should be lesser than the bulk, a fact corroborated by our simulations involving smaller-sized clusters of Pd and Pt where the melting point difference is 190 K [Fig. 10(c)].

D. Effect of graphite support

As indicated by the density profiles, one of the metals in the bimetallics wets the surface more, leading to enriched compositions of the same near the substrate surface. The

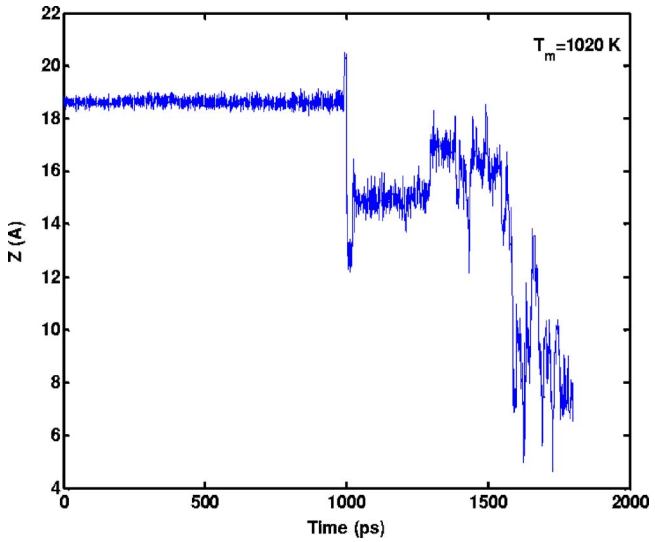

FIG. 11. (Color online) Trajectory of one such copper atom located at surface. The melting point (T_m) of the Pd-Cu cluster is 1020 K.

substrate also delays the onset of surface melting, thereby increasing the overall cluster melting temperature. When the cluster is in a surface-melted state, the effect of the substrate is to pull the loosely bound surface melted atoms. The net effect is to peel off the surface layers of the bimetallic, thus exposing the inner core. This effect is more pronounced at higher compositions of Cu in Cu-Pd and that of Pd in Pd-Pt and Pd-Rh clusters. Figure 11 shows the time evolution of a Cu atom located at the top surface. Each interval of 200 ps corresponds to an increment of 100 K starting at 300 K. Thus, at temperatures much below melting ($<$800 K), the atoms mostly vibrate about their equilibrium temperature, characteristic of solid phase. At slightly higher temperatures close to melting, larger fluctuations and movement are seen. Another striking feature is the reduction in the distance between the surface-segregated metal atom and substrate with an increase in temperature. This behavior is true for all the loosely bound surface atoms.

In case of sensor and catalytic applications, results of energetic studies using DFT indicate the segregation profiles to be reversed on exposure to gases such as CO,[56–59] thereby reducing poisoning. However, the presence of substrate exposes the inner core of surface-melted clusters. Under these conditions, poisonous gases like CO could have serious implications on effectiveness of sensors, especially at higher temperatures.

E. Cluster mobility on graphite substrate

The cluster mobility on the graphite substrate was studied by monitoring the motion of cluster center-of-mass at different temperatures over a time period of 600 ps. As seen from the cluster snapshots, the cluster diffuses as a single entity. At low temperatures, the cluster motion is restricted to less than 1 Å^2, typical of the atomic vibrations in solid phase. After phase transition, cluster movement is over a much larger area ($\sim$90 Å^2). Our calculations indicate that the surface-diffusion coefficient remains low at cluster solid phase (i.e., below 800 K) and increases greatly near the cluster melting point. An increase in the composition of Cu in Pd-Cu and Pd in Pd-Rh leads to higher values of cluster diffusion coefficient, resulting in higher cluster mobility on the graphite substrate. This is attributed to the size mismatch between the metal and carbon atoms at the interface. The inward diffusion of Cu atoms into the cluster core near the melting point changes the interfacial concentration leading to changes in the cluster mobility (diffusion coefficient). The high mobility of the clusters is consistent with experimental results[36] and is likely a result of the size mismatch between the metal and carbon atoms.

V. CONCLUSIONS

The melting characteristics of graphite-supported bimetallic clusters have been studied using MD simulations. The melting points of bimetallic nanoclusters have been found by studying variations in thermodynamic and structural properties with temperature. In all the cases, the effect of the weak graphite support is to delay the onset of melting leading to higher transition temperatures compared with isolated nanoclusters, but still lower than bulk melting points. The delay results from the opposite trends observed in metal-graphite and metal-metal temperature-energy profiles. For all the three nanoclusters, most of the contribution to the total energy and specific-heat capacity arises from metal-metal interactions. The melting temperature depends on nanocluster size and composition with the finite size of nanoclusters, resulting in melting temperatures being different from bulk alloys. Our studies indicate that structural transformations occur at temperatures much below the phase transition. The graphite field causes a rapid rearrangement of atoms located close to the substrate. Bond orientational order parameters suggest a more rapid structural transformation with increasing temperatures in Pd-Cu clusters than Pd-Pt or Pd-Rh nanoclusters. This effect is more pronounced at higher compositions of Cu (Pd-Cu) and Pd (Pd-Pt and Pd-Rh clusters).

The dynamic properties associated with substrate-supported cluster melting were studied using deformation parameters, diffusion coefficients, velocity autocorrelation functions and analysis of density profiles. Components of velocity autocorrelation function characterizing diffusion of the constituent atoms in the bimetallic nanoclusters suggest greater out-of-plane movement in comparison to in-plane, which increases with increasing composition of Cu in Pd-Cu and Pd in Pd-Rh and Pd-Pt. The effect of cluster composition on melting of graphite supported nanoclusters is a nonlinear variation for high Pd composition in the case of Pd-Pt nanoclusters. Supported Pd-Cu and Pd-Rh clusters also exhibit similar characteristics at higher Cu and Pd compositions, respectively. The graphite support serves to reduce the extent of surface melting, thereby introducing nonlinearity. The melting point differences between pure Pd and Pt supported nanoclusters decreases with cluster size. Simulated melting temperatures for bulk alloys agree well with experimental values.

Our studies indicate that wetting behavior is influenced by the weak metal-graphite, and the metal-metal interactions. Influence of the graphite field is restricted to a few monolayers of atoms and has a more prominent effect on surface-melted atoms. Shell-based diffusion coefficients indicate greater surface melting in shells located farther away from the graphite substrate. We find the cluster to diffuse as a single entity on the graphite surface. All the three nanoclusters studied exhibit high diffusivities on the graphite substrate, consistent with experimental observations.

ACKNOWLEDGMENTS

Partial support was provided by NASA-Glenn via FSEC, Florida. The Daresbury laboratory provided the DL_POLY package and the Research Computing Core facility at the University of South Florida provided computational sources, both of which are gratefully acknowledged. The trial version of ACCELRYS (DMOL3) was used to generate the snapshots in Fig. 8. The authors also wish to thank Ling Miao and Reetu Singh for valuable discussions.

*Corresponding author. Electronic address: venkat@eng.usf.edu

[1] A. S. Edelstein and R. C. Cammarata, *Nanomaterials: Synthesis, Properties and Applications* (Institute of Physics, Bristol and Philadelphia, 1996).
[2] A. Chaudhari, MS thesis, USF, 2004.
[3] F. Favier, E. C. Walter, M. P. Zach, T. Benter, and R. M. Penner, Science **293**, 2227 (2001).
[4] J. H. Sinfelt, *Bimetallic Catalysts-Discoveries, Concepts, and Applications* (Wiley, New York, 1983).
[5] S.-P. Huang, D. S. Mainardi, and P. B. Balbuena, Surf. Sci. **545**, 163 (2003).
[6] R. C. Longo, C. Rey, and L. J. Gallego, Surf. Sci. **424**, 311 (1999).
[7] A. Antonelli, S. N. Khanna, and P. Jena, Phys. Rev. B **48**, 8263 (1993).
[8] L. J. Lewis, P. Jensen, N. Combe, and J.-L. Barrat, Phys. Rev. B **61**, 16084 (2000).
[9] L. Bardotti, B. Prevel, P. Melinon, A. Perez, Q. Hou, and M. Hou, Phys. Rev. B **62**, 2835 (2000).
[10] B. Prevel, L. Bardotti, S. Fanget, A. Hannour, P. Melinon, A. Perez, J. Gierak, G. Faini, E. Bourhis, and D. Mailly, Appl. Surf. Sci. **226**, 173 (2004).
[11] W. Vervisch, C. Mottet, and J. Goniakowski, Phys. Rev. B **65**, 245411 (2002).
[12] E. E. Walter, *Metal Clusters*, in Wiley Series in Theoretical Chemistry (Wiley, New York, 1999).
[13] Y. F. Zhukovskii, E. A. Kotomin, D. Fuks, S. Dorfman, and A. Gordon, Surf. Sci. **482**, 66 (2001).
[14] J. P. Borel, Surf. Sci. **106**, 1 (1981).
[15] F. Ercolessi, W. Andreoni, and E. Tosatti, Phys. Rev. Lett. **66**, 911 (1991).
[16] J. W. M. Frenken and J. F. van der Veen, Phys. Rev. Lett. **54**, 134 (1985).
[17] P. Stoltze, J. K. Norskov, and U. Landman, Phys. Rev. Lett. **61**, 440 (1988).
[18] L. J. Lewis, P. Jensen, and J.-L. Barrat, Phys. Rev. B **56**, 2248 (1997).
[19] C. L. Cleveland, W. D. Luedtke, and U. Landman, Phys. Rev. Lett. **81**, 2036 (1998).
[20] Q. Hou, M. Hou, L. Bardotti, B. Prevel, P. Melinon, and A. Perez, Phys. Rev. B **62**, 2825 (2000).
[21] F. Calvo and F. Spiegelmann, J. Chem. Phys. **112**, 2888 (2000).
[22] J. Garcia-Rodeja, C. Rey, L. J. Gallego, and J. A. Alonso, Phys. Rev. B **49**, 8495 (1994).
[23] Y. J. Lee, E. K. Lee, S. Kim, and R. M. Nieminen, Phys. Rev. Lett. **86**, 999 (2001).
[24] D. Bazin, I. Kovacs, J. Lynch, and L. Guczi, Appl. Catal., A **242**, 179 (2003).
[25] D. Bazin, C. Mottet, and G. Treglia, Appl. Catal., A **200**, 47 (2000).
[26] D. Bazin, D. Sayers, J. J. Rehr, and C. Mottet, J. Phys. Chem. B **101**, 5332 (1997).
[27] L. Zhu and A. E. DePristo, J. Chem. Phys. **102**, 5342 (1995).
[28] L. Zhu and A. E. DePristo, J. Catal. **167**, 400 (1997).
[29] F. Rosei, J. Phys.: Condens. Matter **16**, 1373 (2004).
[30] C. Mottet, J. Goniakowski, F. Baletto, R. Ferrando, and G. Treglia, Phase Transitions **77**, 101 (2004).
[31] F. Besenbacher, I. Chorkendorff, B. S. Clausen, B. Hammer, A. M. Molenbroek, J. K. Norskov, and I. Stensgaard, Science **279**, 1913 (1998).
[32] L. Bardotti, B. Prevel, M. Treilleux, P. Melinon, and A. Perez, Appl. Surf. Sci. **164**, 52 (2000).
[33] R. Dolbec, E. Irissou, M. Chaker, D. Guay, F. Rosei, and M. A. El Khakani, Phys. Rev. B **70**, 201406(R) (2004).
[34] S.-P. Huang and P. B. Balbuena, Mol. Phys. **100**, 2165 (2002).
[35] Z. L. Wang, J. M. Petroski, T. C. Green, and M. A. El-Sayed, J. Phys. Chem. B **102**, 6145 (1998).
[36] L. Bardotti, P. Jensen, A. Hoareau, M. Treilleux, and B. Cabaud, Phys. Rev. Lett. **74**, 4694 (1995).
[37] M. Schmidt, R. Kusche, W. Kronmüller, B. von Issendorff, and H. Haberland, Phys. Rev. Lett. **79**, 99 (1997).
[38] L. Yang and A. E. DePristo, J. Catal. **149**, 223 (1994).
[39] W. Smith and T. R. Forester, in *DL_POLY*, edited by W. Smith and T. R. Forester (CCLRC Daresbury Laboratory, Daresbury, Warrington, Cheshire, UK, 1996).
[40] S. M. Foiles, M. I. Baskes, and M. S. Daw, Phys. Rev. B **33**, 7983 (1986).
[41] A. P. Sutton and J. Chen, Philos. Mag. Lett. **61**, 139 (1990).
[42] T. Cagin, Y. Kimura, Y. Qi, L. Yue, I. Hao, H. Ikeda, W. L. Johnson, and W. A. Goddard III, Mater. Res. Soc. Symp. Proc. **554**, 43 (1999).
[43] Y. Qi, T. Cagin, Y. Kimura, and W. A. Goddard III, Phys. Rev. B **59**, 3527 (1999).
[44] Y. Qi, T. Cagin, Y. Kimura, and William A. Goddard III, J. Comput.-Aided Mater. Des. **8**, 233 (2001).
[45] V. R. Bhethanabotla and W. A. Steele, Phys. Rev. B **41**, 9480 (1990).
[46] V. R. Bhethanabotla and W. A. Steele, Langmuir **3**, 581 (1987).
[47] V. R. Bhethanabotla and W. A. Steele, J. Phys. Chem. **92**, 3285 (1988).

[48] V. R. Bhethanabotla and W. A. Steele, J. Chem. Phys. **91**, 4346 (1989).
[49] P. M. Agrawal, B. M. Rice, and D. L. Thompson, Surf. Sci. **515**, 21 (2002).
[50] M. P. Allen and D. J. Tildesley, *Computer Simulation of Liquids* (Oxford University Press, 1987).
[51] T. Morishita, J. Chem. Phys. **113**, 2976 (2000).
[52] T. Iida and R. I. L. Guthrie, *The Physical Properties of Liquid Metals* (Clarendon, Oxford, 1988).
[53] Y. Qi, T. Cagin, W. L. Johnson, and W. A. Goddard III, J. Chem. Phys. **115**, 385 (2001).
[54] P. J. Steinhardt, D. R. Nelson, and M. Ronchetti, Phys. Rev. B **28**, 784 (1983).
[55] S. K. R. S. Sankaranarayanan, V. R. Bhethanabotla, and B. Joseph, Phys. Rev. B **71**, 195415 (2005).
[56] S. Gonzalez, C. Sousa, and F. Illas, Surf. Sci. **531**, 39 (2003).
[57] N. Lopez and J. K. Norskov, Surf. Sci. **477**, 59 (2001).
[58] H. Zhang, Surf. Sci. **269–270**, 331 (1992).
[59] H. Zhang, J. Phys.: Condens. Matter **4**, 529 (1992).